A SURFACE EMG GENERATION MODEL WITH MULTI-LAYER CYLINDRICAL DESCRIPTION OF THE VOLUME CONDUCTOR

Dario Farina, Luca Mesin, Simone Martina, Roberto Merletti

Centro di Bioingegneria, Dip. di Elettronica, Politecnico di Torino, Torino, Italy

Keywords: electromyography, EMG modeling, volume conductor, spatial frequency

Running title: A new model for surface EMG generation

Corresponding author:

Dario Farina, PhD

Dipartimento di Elettronica, Politecnico di Torino; Corso Duca degli Abruzzi 24, Torino, 10129 ITALY

Tel.   0039-0114330476; Fax. 0039-0114330404; e-mail : dario.farina@polito.it

ABSTRACT

We propose a model for surface EMG signal generation with cylindrical description of the volume conductor. The model is more general and complete with respect to previous approaches. The volume conductor is described as a multi-layered cylinder in which the source can be located either along the longitudinal or the angular direction, in any of the layers. The source is represented as a spatio-temporal function which describes the generation, propagation, and extinction of the intra-cellular action potential at the end-plate, along the fiber, and at the tendons, respectively. The layers are anisotropic. The volume conductor effect is described as a two dimensional spatial filtering. Electrodes of any shape or dimension are simulated, forming structures which are described as spatial filters. The analytical derivation which leads to the signal in the temporal domain is performed in the spatial and temporal frequency domains. Numerical issues related to the frequency-based approach are discussed. The descriptions of the volume conductor and of the source are applied to the cases of signal generation from a limb and a sphincter muscle. Representative simulations of both cases are provided. The resultant model is based on analytical derivations and constitutes a step forward in surface EMG signal modeling, including features not described in any other analytical approach.

1. INTRODUCTION

Many methods for the simulation of surface EMG signals have been proposed previously (e.g., [2][4][6][7][11][12][16][17][20][25]). Modeling has been fundamental to investigate the relationships between EMG signal features and the underlying physiological processes. Surface EMG signal modeling has also didactic and many other important applications [26].

In recent years, advances in surface EMG modeling have focused on the description of the volume conductor [2], the detection system [7], and the phenomenon of generation and extinction of the intracellular action potentials at the end-plate and tendons [4]. Both analytical [2][4][6][7][11][20] and numerical [17] approaches have been proposed for the description of the volume conductor. We will refer to analytical approaches when the volume conductor impulse response is provided by a mathematical expression, which depends on the parameters of the system.

Analytical methods are usually computationally more efficient than numerical ones. They also allow an easier interpretation than numerical approaches of the changes of signal features with system parameters. Many theoretical issues related to surface EMG were indeed derived from analytical modeling methods; some examples are the relation between muscle fiber conduction velocity and spectral surface EMG changes during fatigue [16][27], the presence of dips in the frequency bandwidth of EMG signals [16], and the selectivity of EMG detection systems [5][23][24]. Nonetheless, a numerical approach allows description of complex muscle architectures, which is less tenable with analytical derivations.

Recently, Blok et al. [2] analytically described a cylindrical volume conductor that included muscle, fat, and skin layers. Lowery et al. [17] proposed a similar description of the volume conductor, including an internal bone, but used a numerical method instead of an analytical one. We recently presented an approach for surface EMG signal modeling based on the spatial and temporal Fourier frequency characteristics of the signal [7]. This approach was applied to generate signals in a layered (muscle, fat, and skin tissues) volume conductor in Cartesian coordinates with infinite parallel planes separating the tissues. Although this description is rather far from some

experimental conditions, e.g., EMG detection from limb muscles, it may fit well in other cases, e.g., back muscles. The interesting aspect of the model was the new perspective with respect to classic model derivations. The signal in the temporal domain was generated by an equivalent one-dimensional (1-D) filter in the time domain. The latter filter was computed on the basis of the spatial transfer functions of the volume conductor and detection system and of the spatio-temporal function describing the evolution in space and time of the intracellular action potential. This description allowed direct interpretation of surface EMG spectral characteristics. For example, the presence of spectral dips in the case of two-dimensional (2-D) detection systems was investigated theoretically with this modeling approach [7][8]. The model also allowed efficient computation of the simulated potentials by the application of properties of the 2-D Fourier transformation.

A cylindrical volume conductor can be used to describe limb muscles [2] as well as sphincter muscles. In the latter case, the fibers are located around a circumference and the detection system is placed in an internal layer with respect to the source. The description of the volume conductor is similar to the case of the limb but the layers have different conductivities and there is no way of avoiding layers that are internal with respect to that containing the source; the latter characteristic led to numerical problems in the solution of the limb case [2]. The description of the source as well as of the detection modality in the case of modeling a limb or a sphincter is different.

There are no analytical descriptions of the volume conductor representing a limb muscle with layers that are internal with respect to that containing the source and no modeling descriptions of sphincter muscles. We will show that the approach proposed in [7] can be generalized to the case of cylindrical volume conductor. This leads to a very general approach for the simulation of fibers located both along the longitudinal and angular directions. As for the case of infinite parallel planes separating the tissues [7], all the effects of generation and detection of the action potentials will be described by equivalent spatial and temporal filters in the cylindrical volume conductor. No additional computations in the temporal domain are required.

Hence, the main objectives of this study are to: 1) derive an analytical solution that describes the transfer function in the spatial frequency domain of a multi-layer cylindrical volume conductor, with layers both internal and external with respect to that containing the source or the detection system, 2) generalize the approach proposed in [7] for the case of the cylindrical volume conductor investigated, with sources traveling both in the longitudinal and in the angular direction for simulating surface EMG signals generated by a limb or a sphincter muscle, 3) include in the resultant model a complete description of the source (with generation, propagation, and extinction of the intracellular action potentials) and of the detection system, and 4) provide interpretation in the light of sampling of the temporal and spatial domains of the numerical issues related to the implementation of the model in the frequency domain. The developed model is based on analytical derivations and constitutes a step forward in surface EMG signal modeling, including features not described in any other analytical approach. The presented concepts constitute an original and general way of simulating surface EMG signals.

2. METHODS

The investigated geometry is reported in Fig. 1, which describes both the case of a limb and of a sphincter muscle. The coordinates in which the volume conductor is studied are cylindrical (ρ, θ, z). The volume conductor is a multi-layer cylinder with the source located in any of the layers, along the z or θ coordinate. All the layers are limited in the radial direction, i.e., they have finite thickness, except for one which is infinite. The infinite layer may be anisotropic. Different numbers of layers and locations of the detection points lead to different volume conductor models, i.e., different volume conductor transfer functions. In the following, when we refer to the number of layers, we will always include the infinite layer; e.g., a two layer volume conductor model may be constituted by a muscle layer and an infinite air layer.

The source may be in the most internal layer, as in [2], in an intermediate layer, or in the external (infinite) layer. Each layer is homogeneous but may be anisotropic; thus isotropy is not imposed in

any of the layers. This geometry is very general and applies to the case of limb as well as of sphincter muscles. The derivation of the spatial impulse response of the volume conductor is the same in the two cases while the description of the source is different.

In the case of the limb, we assume the source to be placed in an intermediate layer and the recording system to be placed at the boundary between the most external limited layer and the infinite layer (which will be air in this case); in the case of the sphincter, we assume the source to be located in an intermediate or in the infinite layer (which will represent the muscle) and the detection system to be placed at the boundary between the most internal layer (which will be insulating) and the second layer. The intracellular action potentials travel along z or θ, where the fibers are located, in the limb and sphincter case, respectively. Thus, the muscle tissue has higher conductivity in the z or θ direction than in the other directions, in the two cases, respectively.

Since some of the derivations provided below are independent of the coordinate along which the source travels (z or θ), in these cases, we will indicate with x_{lo} and x_{tr} the coordinate longitudinal and perpendicular (transverse) to the muscle fiber direction, respectively. However, the longitudinal coordinate will always be reported as a length, rather than as an angle, to keep the notation uniform. Hence, in the case of the limb, we will have $x_{lo}=z$ and $x_{tr}=\theta$, while, for the sphincter case, $x_{lo}=R\theta$ and $x_{tr}=z$, where R is the radius of the circumference along which the fiber is located (Fig. 1b).

Figure 1 about here

2.1 Source description

A current density source located along one of the spatial coordinates and which originates, propagates, and extinguishes along a finite length muscle fiber, can be described as:

$$i(x_{lo},t) = \frac{d}{dx_{lo}}\left[\psi(x_{lo} - x_{lo\,i} - vt)p_{L_1}(x_{lo} - x_{lo\,i} - L_1/2) - \psi(-x_{lo} + x_{lo\,i} - vt)p_{L2}(x_{lo} - x_{lo\,i} + L_2/2)\right] \quad (1)$$

where t is the time coordinate; $i(x_{lo},t)$ is the current density source; v the velocity of propagation of the source; $\psi(x_{lo})$ the first derivative of $V_m(-x_{lo})$ (with $V_m(x_{lo})$ the intracellular action potential); $p_L(x_{lo})$ a function that takes the value 1 for $-L/2 \leq x_{lo} \leq L/2$ and 0 otherwise; x_{lo_i} the position of the end-plate; L_1 and L_2 the semi-lengths of the fiber from the end-plate to the right and to the left tendon, respectively. This modelization describes sources traveling longitudinally in Cartesian coordinates [7]. Eq. (1) is a generalization of those concepts (see also Fig. 6 in [7]). In the case of the source traveling in the angular direction, we have $x_{lo}=R\theta$, as indicated above. With this notation, Eq. (1) applies for sources propagating both along z and θ. Eq. (1) represents two waves traveling at velocity v in opposite directions, originating at a common point (the end-plate), and extinguishing at distances L_1 and L_2 from the origin.

2.2 Computation of the surface signal in time domain

Assuming that the effects of the volume conductor and detection system can be described as an equivalent 1-D transfer function $B(k_{lo})$ [with corresponding impulse response $b(x_{lo})$] in the spatial domain ($k_{lo} = 2\pi f_{lo}$ is the spatial angular frequency in the longitudinal direction) and considering the potential detected at a specific location $x_{lo} = x_{lo_0}$, we obtain the potential in the time domain as:

$$\varphi(t) = \left(\int_{-s}^{+s} i(x_{lo} - x'_{lo}, t) b(x'_{lo}) \mathrm{d}x'_{lo} \right)_{x_{lo}=x_{lo\,0}} = \left(\int_{-s}^{+s} \int_{-\infty}^{+\infty} i(x_{lo} - x'_{lo}, t - t') b(x'_{lo}) \delta(t') \mathrm{d}x'_{lo} \mathrm{d}t' \right)_{x_{lo}=x_{lo\,0}} =$$

$$\left(\frac{1}{(2\pi)^2} \int_{-\infty}^{+\infty}\int_{-\infty}^{+\infty} I(k_{lo}, k_t) B(k_{lo}) e^{jk_{lo}x_{lo}} e^{jk_t t} \mathrm{d}k_{lo} \mathrm{d}k_t \right)_{x_{lo}=x_{lo\,0}} = \frac{1}{(2\pi)^2} \int_{-\infty}^{+\infty}\int_{-\infty}^{+\infty} I(k_{lo}, k_t) B(k_{lo}) e^{jk_{lo}x_{lo\,0}} e^{jk_t t} \mathrm{d}k_{lo} \mathrm{d}k_t =$$

$$\frac{1}{(2\pi)^2} \int_{-\infty}^{+\infty}\left(\int_{-\infty}^{+\infty} I(k_{lo}, k_t) B(k_{lo}) e^{jk_{lo}x_{lo\,0}} \mathrm{d}k_{lo} \right) e^{jk_t t} \mathrm{d}k_t = \mathfrak{I}_{k_t}^{-1}\left\{ \frac{1}{2\pi} \int_{-\infty}^{+\infty} I(k_{lo}, k_t) B(k_{lo}) e^{jk_{lo}x_{lo\,0}} \mathrm{d}k_{lo} \right\}$$

(2)

where $\mathfrak{I}_{k_t}^{-1}\{\cdot\}$ indicates the inverse Fourier transformation in time domain, $s = \infty$ for propagation along the z axis, $s = R\pi$ for propagation along θ, and with [7]:

$$I(k_{lo}, k_t) = jk_{lo} \frac{1}{v} \Psi^* \left(\frac{k_t}{v} \right) e^{-jk_{lo}x_{lo_i}} \left[e^{-jk_\varepsilon L_1/2} \cdot \frac{\sin(k_\varepsilon L_1/2)}{k_\varepsilon/2} - e^{jk_\beta L_2/2} \cdot \frac{\sin(k_\beta L_2/2)}{k_\beta/2} \right] \qquad (3)$$

where $\Psi \left(\dfrac{k_t}{v} \right)$ is the Fourier transform of $\psi(x_{lo})$ [Eq. (1)] evaluated at $\dfrac{k_t}{v}$; * denotes the complex

conjugate; $k_\varepsilon = k_{lo} + \dfrac{k_t}{v}$, $k_\beta = k_{lo} - \dfrac{k_t}{v}$, and $k_t = 2\pi f_t$ the temporal angular frequency. Note, when

$x_{lo}=R\theta$ in Eqs. (2), that the variable k_{lo} is discrete, due to the periodicity of 2π in θ. Thus, the

integrals in k_{lo} should be interpreted as series. However, the same issue arises when considering the

numerical implementation in which also k_z should assume a finite number of values (see below).

The notation with integrals rather than series can be maintained considering a multiplication of the

argument of the integral by a train of Delta functions which describes in the frequency domain the

periodicity in the angular coordinate. The same notation, which assures uniformity in the

mathematical derivations between the limb and the sphincter case, is used in the section "Derivation

of the spatial transfer function".

Eqs. (2) show that, given the transfer function in the spatial domain, for each instant of time the

potential along the coordinate x_{lo} is computed by a convolution of the spatial impulse response and

the source. If the potential is detected at the point $x_{lo} = x_{lo_0}$, the sampling of the potential can be

seen as an integral in the frequency domain, which is a special case of the Radon transform. These

concepts have been described in detail for a Cartesian coordinate system in [7][8]. Eq. (3) is the 2-D

Fourier transform of the current density source given in (1).

Eqs. (2) are general and allow calculation, through a 1-D inverse Fourier transform, of the potential

generated by the source [Eq. (1)] in a generic volume conductor and detected by a generic detection

system at a specific point along the x_{lo} axis (Fig. 1). The transfer function $B(k_{lo})$ is assumed to be

known and will be calculated below. None of the derivations depends on the propagation axis of the

source.

Fig. 2 shows a block diagram representing this modeling approach. The entire surface EMG generation and detection model is described as the multiplication of two 2-D functions, an integration and a 1-D inverse Fourier transform. This is equivalent to a filtering in the time domain [7].

Figure 2 about here

2.3 Derivation of the spatial transfer function

The function $B(k_{lo})$ in Eqs. (2) represents the transfer function to be applied to a generic source in the spatial domain to compute the spatial potential distribution along the x_{lo} axis, at a transverse distance $x_{tr} = x_{tr_0}$ from the source. (x_{lo_0}, x_{tr_0}) are the coordinates of the detection point (Fig. 1). Assuming an impulsive source in the spatial domain to which the 2-D transfer function $H_{glo}(k_z, k_\theta)$, describing all the spatial phenomena, is applied, the potential detected in the longitudinal direction at the transverse location $x_{tr} = x_{tr_0}$ is:

$$
\varphi(x_{lo}) = \frac{1}{(2\pi)^2} \left(\int_{-\infty}^{+\infty}\int_{-\infty}^{+\infty} H_{glo}(k_z, k_\theta) e^{jk_{lo}x_{lo}} e^{jk_{tr}x_{tr}} dk_{lo}dk_{tr} \right)_{x_{tr}=x_{tr0}} =
$$
$$
= \frac{1}{(2\pi)^2} \int_{-\infty}^{+\infty}\int_{-\infty}^{+\infty} H_{glo}(k_z, k_\theta) e^{jk_{lo}x_{lo}} e^{jk_{tr}x_{tr0}} dk_{lo}dk_{tr} = \mathfrak{I}_{k_{lo}}^{-1}\left\{ \frac{1}{2\pi}\int_{-\infty}^{+\infty} H_{glo}(k_z, k_\theta) e^{jk_{tr}x_{tr0}} dk_{tr} \right\}
$$

(4)

where $\mathfrak{I}_{k_{lo}}^{-1}\{\cdot\}$ stands for the inverse Fourier transformation in the longitudinal spatial coordinate, $H_{glo}(k_z, k_\theta)$ is the 2-D transfer function of the volume conductor and detection system (Fig. 2), $x_{lo} = z$, $x_{tr} = \theta$, $k_{lo} = k_z$, $k_{tr} = k_\theta$, $x_{tr_0} = \theta_0$, for the limb case, and $x_{lo} = R\theta$, $x_{tr} = z$, $k_{lo} = k_\theta/R$, $k_{tr} = k_z$, $x_{tr_0} = z_0$, for the sphincter case. $k_{tr} = 2\pi f_{tr}$ is the spatial angular frequency in the transverse direction. Note that in Eqs. (4), $H_{glo}(k_z, k_\theta)$ is a function of k_z and k_θ for both the limb and the sphincter. This transfer function describes the spatial phenomena related to the volume conductor and detection system, as discussed below. These phenomena do not depend on the propagation

direction of the source. Eqs. (4) indicate that the signal detected along x_{lo} at position $x_{tr} = x_{tr_0}$ and generated by an impulsive source can be viewed as a section of the 2-D inverse Fourier transform of the spatial transfer function of the system. This is equivalent to the 1-D inverse Fourier transform of an integral in the spatial frequency domains, which is again a special case of the Radon transform [7].

From Eqs. (4), the transfer function applied in Eq. (2) is given by (Fig. 2):

$$B(k_{lo}) = \frac{1}{2\pi} \int_{-\infty}^{+\infty} H_{glo}(k_z, k_\theta) e^{jk_{tr}x_{tr_0}} dk_{tr} \tag{5}$$

with $k_{lo} = k_z$, $k_{tr} = k_\theta$, for the limb case, and $k_{lo} = k_\theta/R$, $k_{tr} = k_z$, for the sphincter case.

The previous derivations are extensions of the concepts proposed in [7] to a generation and detection system in a cylindrical coordinate system. With these notations, the model is defined once the volume conductor and the detection system transfer functions have been computed.

2.4 Computation of the transfer function of a multi-layer cylindrical volume conductor

In the following we derive the transfer function of the volume conductor of Fig. 1. The approach includes layers either internal or external to the source, with detection system placed at any layer interface, and describes both limb and sphincter muscles. The notations used are consistent with the description of the source, i.e., the volume conductor is described in k_z and k_θ. Numerical issues related to the sampling of the solution in space and time are treated in the section "Numerical issues".

The electric potential in a volume conductor is obtained from the following relationship in the case of quasi-stationary conditions [3][13][21]:

$$\nabla \cdot J = -\nabla \cdot (\underline{\underline{\sigma}} \nabla \varphi) = I \tag{6}$$

where J is the current density ($A \cdot m^{-2}$), I is the source current density ($A \cdot m^{-3}$), and $\underline{\underline{\sigma}}$ the conductivity tensor.

Considering a cylindrical, homogeneous medium that is symmetric in cylindrical coordinates, and an impulsive source, Eq. (6) becomes:

$$\frac{\sigma_\rho}{\rho}\frac{\partial}{\partial\rho}\left(\rho\frac{\partial\varphi}{\partial\rho}\right)+\frac{\sigma_\theta}{\rho^2}\frac{\partial^2\varphi}{\partial\theta^2}+\sigma_z\frac{\partial^2\varphi}{\partial z^2}=-\frac{1}{\rho}\delta(\rho-R)\delta(\theta)\delta(z) \tag{7}$$

where $(R,0,0)$ are the coordinates of the source in the cylindrical coordinate system and σ_ρ, σ_θ, σ_z are the conductivities in the three coordinates. With the following change of variables:

$$x=k_z\sqrt{\frac{\sigma_z}{\sigma_\rho}}\rho, \tag{8}$$

and assuming that the solution can be written, separating the three variables [14], as the product of three functions in ρ, θ, and z:

$$\varphi(\rho,\theta,z)=\Gamma(\rho)T(\theta)Z(z), \tag{9}$$

we obtain from Eq. (7) the following system in $\Gamma(\rho),T(\theta),Z(z)$:

$$\begin{cases} Z''=-k_z^2Z, \\ T''=-k_\theta^2T, \\ \Gamma''+\dfrac{\Gamma'}{x}-\left(1+\dfrac{\sigma_\theta}{\sigma_\rho}\dfrac{k_\theta^2}{x^2}\right)\Gamma=-\dfrac{1}{\sigma_\rho x_0}\delta(x-x_0). \end{cases} \tag{10}$$

where $x_0=k_z\sqrt{\dfrac{\sigma_z}{\sigma_\rho}}R$ [from Eq. (8)].

The general solution of the system in Eq. (10) is [14]:

$$\begin{cases} Z(z)=z_0e^{jk_zz}+z_1e^{-jk_zz} \\ T(\theta)=T_0e^{jk_\theta\theta}+T_1e^{-jk_\theta\theta} \\ \Gamma(x)=A_n(k_z)I_n(x)+B_n(k_z)K_n(x) \end{cases} \tag{11}$$

where z_0, T_0, z_1, and T_1 are arbitrary constants, $A_n(k_z)$ and $B_n(k_z)$ are arbitrary coefficients,

$n=k_\theta\sqrt{\dfrac{\sigma_\theta}{\sigma_\rho}}$, and $I_n(x)$, $K_n(x)$ are modified Bessel functions of order n of the first and second type, respectively [1]. In Eqs. (11), k_z is a real number while k_θ is an integer number, given the

periodicity of the solution in θ, as discussed above. Substituting Eq. (11) in Eq. (9), we obtain a particular solution of Eq. (7) for each choice of the arbitrary terms $A_n(k_z)$, $B_n(k_z)$, z_0, T_0, z_1, T_1, and for each selection of k_z and k_θ. Due to the linearity of Eq. (7), the general solution can be expressed as a linear combination of the solutions obtained above, yielding the following expression:

$$\varphi(x,\theta,z) = \sum_{k_\theta=-\infty}^{+\infty} \int_{-\infty}^{+\infty} \Gamma(x;k_z,k_\theta)e^{jk_z z}\mathrm{d}k_z e^{jk_\theta \theta} \tag{12}$$

where it has been explicitly stated that the function $\Gamma(x)$ depends on k_z and k_θ, and where the arbitrary constants z_0, T_0, z_1, and T_1 have been included in the coefficients $A_n(k_z)$ and $B_n(k_z)$. From Eq. (12), the potential in the cylindrical coordinate system is obtained as an inverse Fourier transform in k_z and an inverse Fourier series in k_θ. Thus, k_θ is the integer index in the Fourier series. In practical implementations, both k_z and k_θ assume a finite number of values and are, thus, limited. Note also that when the source travels in the θ direction, the longitudinal coordinate is related to k_θ, which is equivalent to k_z when the source travels parallel to the main axis of the cylinder.

The coefficients $A_n(k_z)$ and $B_n(k_z)$ in Eq. (11) should be computed to satisfy the boundary conditions and to allow the discontinuity of the first derivative of $\Gamma(x)$ imposed by the impulsive source. In the general case of N layers with the source located in one of them, there are $2(N+1)$ arbitrary coefficients to be determined, $2(N-1)$ conditions imposing the continuity of the potential and of the flux at the $(N-1)$ interfaces, two conditions imposed by the source, one condition of convergence for $\rho = 0$, and one for $\rho \to \infty$. The conditions at the boundaries of the layers are determined by the following relations [11]:

$$\begin{cases} \Gamma\big|_{\rho_0^+} = \Gamma\big|_{\rho_0^-} \\ \left[\sigma_\rho \dfrac{\partial \Gamma}{\partial \rho}\right]_{\rho_0^+} = \left[\sigma_\rho \dfrac{\partial \Gamma}{\partial \rho}\right]_{\rho_0^-} \end{cases} \tag{13}$$

where ρ_0 indicates the location of the interface under consideration and $\sigma_{\rho_0^+}$, $\sigma_{\rho_0^-}$ are the radial conductivities of the two layers under consideration.

The conditions related to the source are the continuity of the potential and the discontinuity of its first derivative in correspondence of the source [28]:

$$\begin{cases} \Gamma\big|_{x_0^+} = \Gamma\big|_{x_0^-} \\ \Gamma'\big|_{x_0^+} - \Gamma'\big|_{x_0^-} = -\dfrac{1}{\sigma_\rho x_0} \end{cases} \tag{14}$$

with x_0 defined as in Eq. (10) and σ_ρ the radial conductivity of the layer containing the source.

Moreover, to obtain a solution that is internal to the source ($\rho < R$), the coefficient multiplying $K_n(x)$ in Eq. (11), which diverges for $\rho = 0$, should vanish to account for the source being placed in the most internal layer; to obtain a solution that is external to the source ($\rho > R$), the coefficient multiplying $I_n(x)$ in Eq. (11), which diverges for $\rho \to \infty$, should be set to zero to account for the source being in the most external layer. Thus:

$$A_n\big|_{x_0^+} = 0; \quad B_n\big|_{x_0^+} = \frac{1}{\sigma_\rho}I_n(x_0); \quad A_n\big|_{x_0^-} = \frac{1}{\sigma_\rho}K_n(x_0); \quad B_n\big|_{x_0^-} = 0 \tag{15}$$

The following general solution, which is the transfer function of the volume conductor, is obtained in the angular spatial frequency domains k_z and k_θ:

$$\Gamma(\rho, k_z, k_\theta) = A_n(k_z)I_n\left(k_z\sqrt{\frac{\sigma_z}{\sigma_\rho}}\rho\right) + B_n(k_z)K_n\left(k_z\sqrt{\frac{\sigma_z}{\sigma_\rho}}\rho\right) + \begin{cases} \dfrac{1}{\sigma_\rho}I_n\left(k_z\sqrt{\dfrac{\sigma_z}{\sigma_\rho}}R\right)K_n\left(k_z\sqrt{\dfrac{\sigma_z}{\sigma_\rho}}\rho\right) & \text{for} \quad \rho > R \\ \dfrac{1}{\sigma_\rho}K_n\left(k_z\sqrt{\dfrac{\sigma_z}{\sigma_\rho}}R\right)I_n\left(k_z\sqrt{\dfrac{\sigma_z}{\sigma_\rho}}\rho\right) & \text{for} \quad \rho < R \end{cases} \tag{16}$$

with $n = k_\theta\sqrt{\dfrac{\sigma_\theta}{\sigma_\rho}}$. The last term of the solution in Eq. (16) is obtained from Eq. (11) by the source conditions [Eq. (15)] and is different for parts of the volume conductor that are internal and external with respect to the source. In this case, $\rho > R$ is used for the first two conditions in Eq. (15) and $\rho < R$ is used for the third and fourth expressions in Eq. (15).

The transfer function in Eq. (16) is different for the layers that are internal or external to the source. Blok et al. [2] noted that their solution could not work for internal layers but did not generalize their solution to these cases. When there are no layers internal to that of the source and the recording is performed for $\rho > R$, conditions described in Eq. (14) are not used. When modeling structures such as a bone in the limb or a sphincter muscle, the correct solution for layers that are internal to the source is necessary. In particular, the detection is always performed in internal layers for the sphincter (Fig. 1).

In the above derivation, the transfer function was obtained in the two spatial frequency domains. The computation of the signal in time domain, as described in Fig. 2, does not require any calculations in the spatial domain. The truncation of the series in Eq. (12) is viewed in our case as setting the frequency axis to finite limits, which implies a sampling in the spatial domain (see section "Numerical issues"). This applies for both the coordinates. The selection of the frequency axis leads to the same issues, addressed below, in the two spatial domains. Limiting the maximum frequencies, i.e., truncating the series in Eq. (12), does not involve any approximation if the Nyquist theorem is satisfied in all the domains (two spatial and one temporal).

The solution given above does not assume any isotropic layer and can be used in the case of any number of layers. It can be simplified in particular cases. For example, studying a limb and including bone, muscle, fat, skin, and infinite air, we may assume that all the layers are isotropic, except for the muscle. In the case of the sphincter that involves a mucosa and an infinite muscle layer, we set the mucosa to be isotropic and the muscle to be anisotropic. For the isotropic layers, the argument of the Bessel functions in Eq. (16) is $x = k_z \rho$ and the order is $n = k_\theta$. For the limb

muscle tissue, it is $\sigma_\rho = \sigma_\theta < \sigma_z$, $x = k_z \sqrt{\dfrac{\sigma_z}{\sigma_\rho}} \rho$ and $n = k_\theta$. In the case of the sphincter muscle,

the fibers are located around circumferences, hence $\sigma_\rho = \sigma_z < \sigma_\theta$, the argument of the Bessel

functions is $x = k_z \rho$, and $n = k_\theta \sqrt{\dfrac{\sigma_\theta}{\sigma_\rho}}$.

The arbitrary coefficients in Eq. (16) are determined considering the specific cases. In general, they are specified by a linear system that derives from the conditions described in Eqs. (13) and (14):

$$\underline{\underline{A}} \cdot \underline{X} = \underline{b} \tag{17}$$

with $\underline{X}$ the vector of coefficients to be determined and $\underline{\underline{A}}$ and $\underline{b}$ dependent on the volume conductor structure.

In the case of a limb with the bone, muscle, fat, skin, and air, with the layers isotropic except for the muscle, we have:

$$\underline{\underline{A}} = \begin{bmatrix} I_n(ak_z) & -I_n(a_m k_z) & -K_n(a_m k_z) & 0 & 0 & 0 & 0 \\ \sigma_b I_n{'}(ak_z) & -\sqrt{\sigma_{m\rho}\sigma_{mz}}I_n{'}(a_m k_z) & -\sqrt{\sigma_{m\rho}\sigma_{mz}}K_n{'}(a_m k_z) & 0 & 0 & 0 & 0 \\ 0 & I_n(b_m k_z) & K_n(b_m k_z) & -I_n(bk_z) & -K_n(bk_z) & 0 & 0 \\ 0 & \sqrt{\sigma_{m\rho}\sigma_{mz}}I_n{'}(b_m k_z) & \sqrt{\sigma_{m\rho}\sigma_{mz}}K_n{'}(b_m k_z) & -\sigma_f I_n{'}(bk_z) & -\sigma_f K_n{'}(bk_z) & 0 & 0 \\ 0 & 0 & 0 & I_n(ck_z) & K_n(ck_z) & -I_n(ck_z) & -K_n(ck_z) \\ 0 & 0 & 0 & \sigma_f I_n{'}(ck_z) & \sigma_f K_n{'}(ck_z) & -\sigma_s I_n{'}(ck_z) & -\sigma_s K_n{'}(ck_z) \\ 0 & 0 & 0 & 0 & 0 & \sigma_s I_n{'}(dk_z) & \sigma_s K_n{'}(dk_z) \end{bmatrix};$$

$$\underline{b} = \begin{bmatrix} \dfrac{I_n(a_m k_z)K_n(R_m k_z)}{\sigma_{m\rho}} \\[2mm] \sqrt{\dfrac{\sigma_{mz}}{\sigma_{m\rho}}}I_n{'}(a_m k_z)K_n(R_m k_z) \\[2mm] -\dfrac{I_n(Rk_z)K_n(b_m k_z)}{\sigma_{m\rho}} \\[2mm] -\sqrt{\dfrac{\sigma_{mz}}{\sigma_{m\rho}}}I_n(R_m k_z)K_n{'}(b_m k_z) \\[2mm] 0 \\ 0 \\ 0 \end{bmatrix}; \quad \underline{X} = \begin{bmatrix} A_n^1(k_z) \\ A_n^2(k_z) \\ B_n^2(k_z) \\ A_n^3(k_z) \\ B_n^3(k_z) \\ A_n^4(k_z) \\ B_n^4(k_z) \end{bmatrix}; \tag{18}$$

with $n = k_\theta$ and with the following notations:

$$R_m = \sqrt{\frac{\sigma_{mz}}{\sigma_{m\rho}}}R; a_m = \sqrt{\frac{\sigma_{mz}}{\sigma_{m\rho}}}a; b_m = \sqrt{\frac{\sigma_{mz}}{\sigma_{m\rho}}}b;$$

$$I_n{'}(x) = \frac{dI_n(x)}{dx} = \frac{I_{n+1}(x) + I_{n-1}(x)}{2}; K_n{'}(x) = \frac{dK_n(x)}{dx} = -\frac{K_{n+1}(x) + K_{n-1}(x)}{2} \tag{19}$$

being a, b, c, and d defined in Fig. 1, σ_b, σ_{mz}, $\sigma_{m\rho}$, σ_f, and σ_s the conductivities of the bone, of the muscle in longitudinal and radial direction, of the fat, and skin, respectively.

In the case of the sphincter muscle, assuming an infinite external muscle layer (anisotropic), an intermediate layer modeling the mucosa (isotropic), and an internal non-conductive layer where the detection probe is placed, we have:

$$\underline{\underline{A}} = \begin{bmatrix} I_n'(ak_z) & K_n'(ak_z) & 0 \\ I_n(bk_z) & K_n(bk_z) & -K_p(bk_z) \\ \sigma_\mu I_n'(bk_z) & \sigma_\mu K_n'(bk_z) & -\sigma_{mp} K_p'(bk_z) \end{bmatrix}, \quad \underline{b} = \begin{bmatrix} 0 \\ \dfrac{I_p(bk_z)K_p(Rk_z)}{\sigma_{mp}} \\ I_p'(bk_z)K_p(Rk_z) \end{bmatrix}, \quad \underline{X} = \begin{bmatrix} A_n^1(k_z) \\ B_n^1(k_z) \\ A_p^2(k_z) \end{bmatrix} \quad (20)$$

with the notations of Eq. (19), σ_μ the conductivity of the mucosa, $n = k_\theta$, $p = k_\theta \sqrt{\dfrac{\sigma_{m\theta}}{\sigma_{m\rho}}}$, $\sigma_{m\theta}$ and

$\sigma_{m\rho}$ the conductivities of the muscle in the angular and radial direction, respectively.

For both the limb and sphincter, determination of the arbitrary coefficients given above can be generalized to any number of layers and location of the source. Note that Eqs. (13, 14, 15, 16) determine a system of equations for the determination of the arbitrary coefficients that is different to the description by Gootzen [11] when there are layers internal to the source. Figs. 3 and 4 show the impulse responses computed as described above for the limb and sphincter case with different numbers of layers. Although impulse responses were not used in any of the modeling derivations because all the calculations are performed in the frequency domain (Fig. 2), they are shown here for clarity, due to the ease with which they can be interpreted. In Fig. 3, note that the addition of isotropic layers reduces the frequency support in the angular direction, which corresponds to poorer selectivity in the corresponding spatial direction.

Figures 3 and 4 about here

2.5 Numerical issues

The arbitrary coefficients in Eq. (16) are obtained from the system described in Eq. (17) for each value of k_z and k_θ, which are both discrete in the numerical implementation. Given the symmetry of the volume conductor, the transfer function represented by Eq. (16) is symmetric with respect to k_z

16

and k_θ. Thus, the transfer function of the volume conductor has to be computed only for positive values of the two frequencies which leads to a reduction to one fourth of the number of systems in Eq. (17) that should be solved.

Numerical problems may arise in the inversion of the ill-conditioned matrix $\underline{\underline{A}}$, as indicated for the case of two layers plus air in [11]. To reduce the conditioning number for the inversion of the matrix $\underline{\underline{A}}$, we propose the following substitution of the vector $\underline{X}$, which is derived from the method proposed in [11]:

$$\underline{X}'=\begin{bmatrix} A_n^1(k_z)I_n(k_z a) \\ A_n^2(k_z)I_n(k_z b_m) \\ B_n^2(k_z)K_n(k_z b_m) \\ A_n^3(k_z)I_n(k_z c) \\ B_n^3(k_z)K_n(k_z c) \\ A_n^4(k_z)I_n(k_z d) \\ B_n^4(k_z)K_n(k_z d) \end{bmatrix} \tag{21}$$

for the case described in Eq. (18) and

$$\underline{X}'=\begin{bmatrix} A_n^1(k_z)I_n(k_z a) \\ B_n^1(k_z)K_n(k_z a) \\ B_p^2(k_z)K_p(k_z b) \end{bmatrix} \tag{22}$$

for the case represented in Eq. (20). Eqs. (21) and (22) are related to Eqs. (18) and (20), but can be extended to any number of layers and position of the source. The entries of the matrix $\underline{\underline{A}}$ are changed accordingly. With the substitutions described in Eqs. (21) and (22), the conditioning number for the inversion of $\underline{\underline{A}}$ reduces by some orders of magnitude with respect to the technique proposed in [11] and [2], providing more stable solutions, even for the case of many layers (see also "Results").

For the numerical implementation of the model, as described in Fig. 2, sampling of the frequency coordinate systems implies periodic repetition of the solution in the spatial and temporal domains, and vice versa.

The longitudinal coordinate (along which the source travels) and time are linked by the propagation velocity:

$$x_{lo} = vt \tag{23}$$

where v is the conduction velocity. A similar relation occurs between the spatial frequency and the time frequency domains ($k_{lo} = \frac{1}{v} k_t$). In the time domain, the frequency bandwidth is limited to the interval [$-f_{samp}/2, +f_{samp}/2$], with f_{samp} being the sampling frequency of the simulated signal. Thus, with $k_{lo_{max}}$ as the maximal angular spatial frequency, we get:

$$k_{lo_{max}} = \pi \frac{f_{samp}}{v} \tag{24}$$

The spatial frequency is also discrete with steps:

$$\Delta k_{lo} = \frac{2k_{lo_{max}}}{w} \tag{25}$$

where Δk_{lo} is the frequency resolution and w is the number of spatial frequency bins used in the numerical implementation. We also have, from the sampling of k_{lo}, a limit to the interval of definition of x_{lo}:

$$x_{lo_{max}} = \frac{1}{\pi \Delta k_{lo}} \tag{26}$$

$$\Delta x_{lo} = \frac{1}{\pi k_{lo_{max}}} \tag{27}$$

Outside the interval $[-x_{lo_{max}}, +x_{lo_{max}}]$, the impulse response of the volume conductor is repeated periodically in the longitudinal direction. In the θ direction this reflects the physical periodicity of the volume conductor with the condition $x_{lo_{max}} = \pi$, which is imposed by the physical structure. For a limb, the repetition of the impulse response function is equivalent to doubling the potential at the longitudinal borders which is the same as applying the image theorem and modeling a limited

volume conductor in the z direction [2]. In the latter case, the length of the limb in z can be fixed by selecting an appropriate value of w.

From Eqs. (24, 25, 26), the parameter w (number of bins in the frequency axis) is given by:

$$w = \frac{2k_{lo_{max}} x_{lo_{max}}}{\pi} = \frac{2x_{lo_{max}} f_{samp}}{v} \tag{28}$$

For example, with sampling frequency f_{samp} = 4096 Hz, z_{max} = 125 mm and v = 4 m/s, we get, for the limb muscle, $k_{z,max} = 2\,\pi\,512$ m^{-1}, w = 256, $\Delta k_z = 2\,\pi\,4$ m^{-1}, and Δz = 0.977 mm.

In the case of the sphincter muscle, $x_{lo_{max}} = \pi$ and Eq. (28) becomes:

$$w = \frac{2\pi f_{samp}}{v} \tag{29}$$

In practice, the number of frequency points is then reduced to $w/2$, due to the symmetry of the solution.

The limitation of the spatial coordinate θ to the interval $[-\pi, +\pi]$ imposes a sampling of the spatial frequency, as in the case of the z coordinate. Eq. (27) also describes the effect of limiting to a finite frequency. This implies a sampling in the spatial and, thus, temporal domains.

The same problems of limitation and sampling occur for the transverse coordinate; in this case, however, space and time are not linked by the propagation velocity. The above derivations show that the sampling problem is the same for the two spatial dimensions in practical cases. Truncation of the series in Eq. (12) is viewed with our approach as a limitation of the frequency axis, which implies sampling in the spatial domain. This sampling should be done in agreement with the Nyquist theorem and in this case does not imply any approximation of the solution.

2.6 Electrode configuration and physical dimensions of the electrodes

Considering the linear summation of signals detected by different point electrodes, we obtain a spatial filter [24][25] whose transfer function $H_{sf}(k_z, k_\theta)$ is given by:

$$H_{sf}(k_z, k_\theta) = \sum_{i=-l}^{q-1} \sum_{u=-g}^{h-1} a_{iu} e^{-jk_z id_z} e^{-jk_\theta u d_\theta} \tag{30}$$

with l, q, h, g positive integers ($l+q$ is the number of electrodes in the z direction and $h+g$ the number of electrodes in the θ direction), a_{iu} the weights given to the electrodes, d_z and d_θ the interelectrode distances in the two directions. Assuming a matrix of electrodes that can be adapted to the shape of the volume conductor, the distance d_θ in Eq. (30) is given by:

$$d_\theta = \frac{d}{R_{ele}} \tag{31}$$

where d is the distance between the electrodes and R_{ele} is the radius of the circumference along which the electrodes placed along θ are located. Note that Eq. (31) derives from the convention of Eq. (30) which assumes the angular spatial frequencies related to z and θ, thus d_θ should be expressed in radians. These notations are in line with the previous derivations.

The transfer function $H_{size}(k_z, k_\theta)$ describing the electrode shape can be derived as proposed in [7] and adapted to the particular geometry of the volume conductor. The method adopted for the description of the effect of electrodes of physical dimensions proposed in [7] assumes that the potential distribution under the electrode area is integrated by the electrode, which, as indicated in [7], is valid as a first approximation. The correct description of electrodes with physical dimensions would imply the solution of a mixed boundary condition problem. Assuming a simple integration, for rectangular electrodes we obtain the following transfer function:

$$H_{size}(k_z, k_\theta) = \mathrm{sinc}\left(\frac{k_\theta a_{ele}}{2\pi R_{ele}}\right) \mathrm{sinc}\left(\frac{k_z b_{ele}}{2\pi}\right) \tag{32}$$

with a_{ele} and b_{ele} the length of the edges of the electrode and $\mathrm{sinc}(x) = \sin(\pi x)/(\pi x)$ if $x \neq 0$, $\mathrm{sinc}(0) = 1$.

For elliptical/circular electrodes:

$$H_{size}(k_z, k_\theta) = \begin{cases} 2\dfrac{J_1(\sqrt{(a_{ele}k_\theta/R_{ele})^2 + (b_{ele}k_z)^2})}{\sqrt{(a_{ele}k_\theta/R_{ele})^2 + (b_{ele}k_z)^2}} & for \quad (k_z, k_\theta) \neq (0,0) \\ 1 & for \quad (k_z, k_\theta) = (0,0) \end{cases} \tag{33}$$

where $J_1(x)$ is the Bessel function of the first order [1] and a_{ele} and b_{ele} the semi-axes of the elliptical electrode ($a_{ele} = b_{ele} = r_{ele}$ in case of a circular electrode of radius r_{ele}). Any other electrode shape can be described adapting the concepts presented in [7].

The transfer function $H_{ele}(k_z, k_\theta)$ describing the spatial filtering and the electrode shape is thus:

$$H_{ele}(k_z, k_\theta) = \sum_{i=-l}^{q-1} \sum_{u=-g}^{h-1} a_{iu} H_{size}^{iu}(k_z, k_\theta) e^{-jk_z i d_z} e^{-jk_\theta u d_\theta} \tag{34}$$

with d_θ given by (31) and $H_{size}^{iu}(k_z, k_\theta)$ the transfer function describing the shape of the electrode with weight a_{iu} of the spatial filter.

If the detection system is inclined with respect to the fiber, the transfer function (34) is also rotated in the frequency domain. In Cartesian coordinates, the rotation by the angle α is given by the following change of variables:

$$\begin{cases} z' = -\sin(\alpha)x + \cos(\alpha)z \\ x' = \cos(\alpha)x + \sin(\alpha)z \end{cases} \tag{35}$$

The corresponding changes of variables in the coordinates (z, θ) is obtained from Eq. (35) with the substitutions $x = R_{ele}\theta$, $x' = R_{ele}\theta'$:

$$\begin{cases} z' = -R_{ele}\sin(\alpha)\theta + \cos(\alpha)z \\ \theta' = \cos(\alpha)\theta + \sin(\alpha)z/R_{ele} \end{cases} \tag{36}$$

Applying the transformation described in Eq. (36), the transfer function represented in Eq. (34) may be written as:

$$H_{ele}(k_z, k_\theta, \alpha) = \iint h_{ele}(z', \theta') e^{-jk_\theta \theta'} e^{-jk_z z'} d\theta' dz' =$$

$$= \iint h_{ele}(z, \theta) e^{-jk_\theta(\theta\cos(\alpha)+z\sin(\alpha)/R_{ele})} e^{-jk_z(-R_{ele}\theta\sin(\alpha)+z\cos(\alpha))} d\theta dz = \iint h_{ele}(z, \theta) e^{-jk'_\theta \theta} e^{-jk'_z z} d\theta dz \tag{37}$$

with:

$$\begin{cases} k'_z = \dfrac{1}{R_{ele}} k_\theta \sin(\alpha) + k_z \cos(\alpha) \\ k'_\theta = k_\theta \cos(\alpha) - k_z R_{ele} \sin(\alpha) \end{cases} \tag{38}$$

Eqs. (38) represent the transformation that should be applied to the spatial frequency domain to account for the inclination of the detection system with respect to the fiber. Application of the transformation in Eq. (38) to Eq. (34) will produce a transfer function in k_z and k_θ that accounts for electrodes of finite dimensions (first approximation with integration), arranged in different configurations, and with an eventual inclination with respect to the axis of propagation of the source.

$H_{glo}(k_z,k_\theta)$ in Eq. (5) is the multiplication of the transfer function of the volume conductor $H_{vc}(k_z,k_\theta) = \Gamma(\rho, k_z, k_\theta)$ [Eq. (16)] and the transfer function of the detection system $H_{ele}(k_z,k_\theta)$ [Eq. (34) with change of variables (38)] (Fig. 2). The simulated signal in time domain is then obtained from Eqs. (2).

3. RESULTS

The concepts described above have been included in a model of surface EMG signal generation which simulates single muscle fiber as well as motor unit action potentials. Consequently, the model is a filtering operation in the time domain [Eqs. (2)]. The model also includes the possibility of summing together motor unit action potentials with the corresponding firing patterns and thereby describing the complete generation of the interference surface EMG signal, as described in [9][10]. Fig. 5 shows examples of simulated signals from a limb muscle in the case of two (muscle and air) and five (bone, muscle, fat, skin, and air) layers. Monopolar and single differential recordings are performed in transverse locations around the limb.

With the derivation provided and with the numerical implementation proposed, we did not find any problem of convergence for the solution, even adding another internal layer in addition to the bone (thus having six layers in total, two internal, one containing the source, and three external with

respect to the source). We tested the analytical solutions for different numbers of layers by comparing the results of a structure with *N* layers with those of a model with one more layer whose thickness tended to zero. All the solutions were stable for any position of the source.

Fig. 6 reports examples of simulated signals generated by a sphincter muscle. Note the different time needed for the potentials to extinguish at the tendons depending on the depth of the source. Conduction velocity is thus apparently lower for deeper motor units. Signals of similar characteristics have been detected in previous experimental work from sphincter and urethral muscles [18][19]. In particular, experimental recordings from sphincter muscles often showed potentials with very low apparent conduction velocity [18], which can be interpreted on the basis of the present model. Indeed, the delay between action potentials recorded from electrodes placed along a circumference is related to the angular velocity of propagation, which depends on the radius of the circumference along which the source travels. A motor unit action potential recorded experimentally from the anal sphincter is also reported in Fig. 6 as a representative example of signal features.

Figures 5 and 6 about here

4. DISCUSSION AND CONCLUSIONS

In this study we proposed a general approach for modeling the generation of the surface EMG signal. The adaptation of the modeling concepts proposed in [7] to a cylindrical volume conductor and to sources traveling both in the z and θ direction shows that those concepts represent a very general way of interpreting surface EMG signal generation. Fig. 2 represents the entire model in which each block can be changed according to the specific anatomical conditions and detection system parameters. The volume conductor may be either cylindrical, which we focused on in this work, or comprised of parallel planes, as described in [7], allowing simulation of a large range of anatomical conditions.

The proposed model is more general than previous ones. It allows the description of 1) any current density source, 2) a cylindrical volume conductor of a number of layers with the source either in an internal, intermediate or external infinite layer, 3) layers that are anisotropic in the three directions, 4) sources traveling either in the longitudinal (z) or in the angular (θ) direction, 5) any kind of detection system, including electrodes of any shape and any spatial-filtering characteristics, and 6) the generation and extinction of the intracellular action potential at the end-plate and tendons by progressive appearing and extinguishing of the potential, without any approximation with equivalent sources. The model is analytical and designed entirely in the Fourier domains, spatial and temporal. The simulated potentials are given by a 1-D inverse Fourier transform of a function in the temporal frequency domain, obtained by spatial and temporal filtering operations on the current density source [Eq. (2) and Fig. 2]. The numerical issues related to this approach have been addressed. The inherent periodic repetition of the solution in the spatial domain implies constraints in the selection of the frequency bins. Given the frequency axis sampling and limitation, the two spatial frequencies have equivalent properties and can be viewed in the same way, assuming a sampling and a periodic repetition of the solution. Periodicity is inherently present in the angular direction while it is imposed by the numerical implementation in the z direction. Constraints on the sampling intervals are also imposed by the relation between the temporal domain and the longitudinal spatial coordinate. The longitudinal coordinate may be either z or θ. No approximations are introduced at any step of the numerical implementation of the model if the Nyquist sampling limit is satisfied in the spatial and temporal coordinate systems.

The generation and extinction phenomena are not described as equivalent sources, as in other models [2][11][12][15][17], but a progressive appearing and disappearing of the first derivative of the intracellular action potential at the end-plate and tendons is simulated.

The description of the volume conductor includes both limb and sphincter muscles. For the limb case, there are no reports in the literature in which the bone, muscle, fat, and skin layers have been described analytically. With respect to this, we also obtained stable solutions with an additional

internal layer, leading to a model with the bone divided in an internal and a cortical part. Blok et al. [2] indicated that the inclusion of an internal layer with respect to the muscle in their model produced oscillations in the solution. In the present work, we simulated limb muscles with layers internal or external with respect to the source. Moreover, we also analyzed sphincter muscles, which have never been simulated before, for which the fiber is always in a layer external to the site of signal detection. The generalization of the approach allows the use of different transfer functions to represent the volume conductor with the same description of the generation phenomena and detection modalities provided in this study.

The main contribution of this work is thus to present a method for the simulation of surface EMG signals, which allows a general description of the signal source and of the detection system in a complex cylindrical volume conductor. We provided an analytical solution for the description of a cylindrical volume conductor with many layers, with the source and the detection system placed in any of the layers. The approach can be extended to different volume conductor models, such as one comprised of infinite parallel layers [7]. The generality of the approach led to a similar treatment of sources traveling along z or θ, with similar concepts related to the description of the source and to the numerical implementation of the solution.

REFERENCES

1. M. Abramowitz, I.A. Stegun, *Handbook of mathematical functions*, Dover, 1965

2. J.H. Blok, D.F. Stegeman, A. van Oosterom, "Three-layer volume conductor model and software package for applications in surface electromyography," *Ann. Biomed. Eng.*, vol. 30, pp. 566-577, 2002

3. J. Clark, R. Plonsey, "The extracellular potential field of the single active nerve fiber in a volume conductor," *Biophys. Journ.*, vol. 8, pp. 842-64, 1968

4. G.V. Dimitrov, N.A. Dimitrova, "Precise and fast calculation of the motor unit potentials detected by a point and rectangular plate electrode," *Med. Eng. & Phys.*, vol. 20, pp. 374-381, 1998

5. C. Disselhorst, J. Silny, G. Rau, "Improvement of spatial resolution in surface-EMG: a theoretical and experimental comparison of different spatial filters," *IEEE Trans. Biomed. Eng.*, vol. 44, pp. 567-574, 1997

6. J. Duchene, J.Y. Hogrel, "A model of EMG generation," *IEEE Trans. Biomed. Eng.*, vol. 47, pp. 192-201, 2000

7. D. Farina, R. Merletti, "A novel approach for precise simulation of the EMG signal detected by surface electrodes," *IEEE Trans. Biomed. Eng.*, vol. 48, pp. 637-646, 2001

8. D. Farina, R. Merletti, "Effect of electrode shape on spectral features of surface detected motor unit action potentials," *Acta Physiol. Pharmacol. Bulg.*, vol. 26, pp. 63-66, 2001

9. D. Farina, M. Fosci, R. Merletti, "Motor unit recruitment strategies investigated by surface EMG variables," *Journ. Appl. Physiol.*, vol. 92, pp. 235-247, 2002

10. D. Farina, L. Fattorini, F. Felici, G. Filligoi, "Nonlinear surface EMG analysis to detect changes of motor unit conduction velocity and synchronization," *Journ. Appl. Physiol.*, vol. 93, pp. 1753-1763, 2002

11. T.H. Gootzen, "Muscle fibre and motor unit action potentials. A biophysical basis for clinical electromyography," PhD thesis, University of Nijmegen, 1990

12. T.H. Gootzen, D.F. Stegeman, A. Van Oosterom, "Finite limb dimensions and finite muscle length in a model for the generation of electromyographic signals," *Electroenc. Clin. Neurophysiol.*, vol. 81, pp. 152-162, 1991

13. A. Heringa, D.F. Stegeman, G.J. Uijen, J.P. de Weerd, "Solution methods of electrical field problems in physiology," *IEEE Trans. Biomed. Eng.*, vol. 29, pp. 34-42, 1982

14. J.D. Jackson. Classical Electrodynamics. John Wiley & Sons, New York, 1975

15. P. Kleinpenning, T. Gootzen, A. Van Oosterom, D.F. Stegeman, "The equivalent source description representing the extinction of an action potential at a muscle fiber ending," *Math. Biosci.*, vol. 101, pp. 41-61, 1990

16. L. Lindstrom, R. Magnusson, "Interpretation of myoelectric power spectra: a model and its applications," *Proc. IEEE*, vol. 65, pp. 653-662, 1977

17. M.M. Lowery, N.S. Stoykov, A. Taflove, T.A. Kuiken, "A multiple-layer finite-element model of the surface EMG signal," *IEEE Trans. Biomed. Eng.*, vol. 49, pp. 446-454, 2002

18. R. Merletti, P. Enck, M. Gazzoni, H. Hinninghofen, "Surface EMG recording of single motor unit action potentials from the external anal sphincter," *Proc. XIV ISEK Congress*, Vienna, 2002, pp. 23-24

19. R. Merletti, D. Farina, M. Gazzoni, "The linear electrode array: a useful tool with many applications," *Journ. Electromyogr. Kinesiol.*, vol. 13, pp. 37-47, 2003

20. R. Merletti, L. Lo Conte, E. Avignone, P. Guglielminotti, "Modelling of surface EMG signals. Part I: model and implementation," *IEEE Trans. on Biomed. Eng.*, vol. 46, pp. 810-820, 1999

21. R. Plonsey, "Action potential sources and their volume conductor fileds," *IEEE Trans. on Biomed. Eng.*, vol. 56, pp. 601-611, 1977

22. P. Rosenfalck, "Intra and extracellular fields of active nerve and muscle fibers. A physico-mathematical analysis of different models," *Acta Physiol. Scand.*, vol. 321, pp. 1-49, 1969

23. H. Reucher, G. Rau, J. Silny, "Spatial filtering of noninvasive multielectrode EMG: Part I--Introduction to measuring technique and applications," *IEEE Trans. Biomed. Eng.*, vol. 34, pp. 98-105, 1987

24. H. Reucher, J. Silny, G. Rau, "Spatial filtering of noninvasive multielectrode EMG: Part II--Filter performance in theory and modeling," *IEEE Trans. Biomed. Eng.*, vol. 34, pp. 106-113, 1987

25. J. Schneider, J. Silny, G. Rau, "Influence of tissue inhomogeneities on noninvasive muscle fiber conduction velocity measurements investigated by physical and numerical modeling," *IEEE Trans. on Biomed. Eng.*, vol. 38, pp. 851-860, 1991

26. D.F. Stegeman, J.H. Blok, H.J. Hermens, K. Roeleveld, "Surface EMG models: properties and applications," *Journ. Electromyogr. Kinesiol.*, vol. 10, pp. 313-26, 2000

27. F.B. Stulen, C.J. DeLuca, "Frequency parameters of the myoelectric signal as a measure of muscle conduction velocity," *IEEE Trans. Biomed. Eng.*, vol. 28, pp. 515-523, 1981

28. P.R. Wallace. Mathematical Analysis of Physical Problems. Dover, 1984

FIGURE CAPTIONS

Fig. 1 (a) The investigated layered volume conductor. The most external infinite layer can be air or a tissue of any conductivity. The source (muscle fiber) may be located both in the z and in the θ direction, is of finite length, and may be placed in any of the layers. The layers have conductivities which, in general, may be different in the three spatial directions. The detection points may be at the interface of any two layers. (b) A section of the volume conductor shown in (a). In (a) and (b) two fibers are reported, corresponding to the case of propagation in the longitudinal and angular direction (indicated as Source 1 and 2). The radial distance of the fibers from the center of the volume conductor is indicated with R_1 and R_2 for Source 1 and 2, respectively. L_1 and L_2 are lengths of the fibers from the end-plate to the tendon (semi-lengths). The number of layers may be increased or decreased with respect to those shown in the figure. Both Source 1 and 2 can be located in different layers with respect to what is shown. Two possible locations of the detection points are shown. a, b, c, and d are the radial distances defining the interfaces between layers. z_0 and θ_0 are the z and θ coordinates of the detection point.

Fig. 2 a) A general schematic representation of the model, containing the description of the volume conductor, fibers of finite length, and the detection system. Given the transfer function $B(k_{lo})$, which represents all the spatial related phenomena, the calculations to obtain the simulated signal in time domain are entirely performed in the frequency domain (spatial and temporal). The final simulated signal is the 1-D inverse Fourier transform of the integral of a 2-D function in the spatial and temporal frequency domain. The scheme is derived from the concepts proposed in [7] and is adapted to the cylindrical coordinate system. b) The scheme describing how $B(k_{lo})$ is obtained. $H_{vc}(k_z,k_\theta)$ is the transfer function of the volume conductor, $H_{sf}(k_z,k_\theta)$ of the spatial filter, $H_{size}(k_z,k_\theta)$ of the electrode shape (see text for details). The notations in this case are $k_z = k_{lo}$, $k_\theta = k_{tr}$ for the limb case, and $k_\theta = Rk_{lo}$, $k_z = k_{tr}$ for the sphincter case, with R the radial distance

of the source from the origin of the coordinate system and $k_{tr} = 2\pi f_{tr}$ the spatial angular frequency in the transverse direction.

Fig. 3 The impulse response of the volume conductor describing a limb, in the case of two layers (muscle and air) (a) and five layers (bone, muscle, fat, skin, and air) (b). In the case of (b), the thickness of the skin layer (isotropic, conductivity 1 S/m) was 2 mm, the fat layer (isotropic, conductivity 0.05 S/m) was 3 mm, the muscle tissue (anisotropic, longitudinal conductivity 0.5 S/m, radial and angular conductivities 0.1 S/m) was 25 mm, and the bone (isotropic, conductivity 0.02 S/m) had a radius of 20 mm. In the case of (a), the muscle had the same properties as in (b) and a radius of 50 mm. The potential distribution is detected at the interface between the air and the muscle in (a) or the skin in (b). The fiber is at a distance of 6 mm from the detection surface in both cases.

Fig. 4 The impulse response of the volume conductor describing a sphincter with three layers (internal insulating, mucosa, semi-infinite muscle). The mucosa (2 mm thick) has the same conductivity properties as the skin layer in Fig. 3, while the muscle has its greatest conductivity in the angular direction. The internal insulating layer has a radius of 7 mm, and the fiber is 1 mm deep within the muscle.

Fig. 5 Examples of simulated monopolar and single differential muscle fiber action potentials in the case of limb muscle with (a) two layers (muscle and air) and (b) five layers (bone, muscle, fat, skin, and air). The potentials are detected in five (to the left and right) locations around the limb circumference. The locations are 5 degrees apart. The conductivities and thickness of the different layers are the same as in Fig. 3. Two fibers (F1 and F2) were simulated at a depth of 1 and 5 mm within the muscle in (b) and 6 mm and 10 mm within the muscle in (a). The total distance between the sources and the detection points is the same in (a) and (b). The fibers have semi-lengths 50 mm and 40 mm, the detection system is placed over the shorter semi-length, at a distance of 20 mm from the end-plate. For the single differential recording, the interelectrode distance is 5 mm. In all cases, the current density source is described as proposed in [22] (see also [7]) and conduction

velocity was 4 m/s. Point electrodes have been simulated in all cases. Note the presence of both propagating and end-of-fiber signal components, especially in the case of monopolar recordings. Note also the different rate of decrease with increasing distance from the source between propagating and end-of-fiber components and between the two- and the five-layer case. The potentials in (a) and (b) are normalized with respect to the amplitude of the largest potential in (a) and (b), respectively.

Fig. 6 Examples of monopolar [(b), (c)] and single differential [(e), (f)] simulated signals in the case of the sphincter muscle, with the geometry represented in (a). In (a) the numbers 1, …, 16 indicate the electrodes, i.e., the detection points for monopolar recordings, while the letters A, …, R indicate the middle points between two consecutive electrodes, i.e., the detection points for the single differential recordings. The model assumes an internal insulating layer, mucosa, and the infinite muscle layer with the same properties as in Fig. 4. Two fibers (F1 and F2) at a depth of 1 mm and 4 mm within the muscle, with the same conduction velocity of 2.3 m/s, have been simulated. The lengths of the two fibers are different, so that they start and end at the same angles (total angular length 200 degrees). Location of end-plates and tendons is indicated. In all cases, the current density source is described as proposed in [22] (see also [7]) and point electrodes have been simulated. Note the apparently different velocity of propagation of the two fibers when observing the simulated signals. This is due to the fact that the angular velocity, which is observed by the simulated detection system, is different in the two cases. In all cases, the potentials are normalized with respect to their maximum values, thus their amplitudes can not be compared. In (d) a motor unit action potential extracted from experimental signals is shown. The signals have been detected from the anal sphincter of a healthy male subject using a cylindrical probe of 14 mm diameter. 16 silver contact bars 10 mm long (transverse muscle fiber direction) and 1 mm diameter are equally spaced around the circumference of the probe. Single differential technique is used for signal detection. Contact 1 and 16 are dorsal and 8 is ventral. A maximal voluntary contraction is produced by the subject. There was no attempt to match the experimental signals with the modeling ones. The real

signals are reported only as representative examples of the features of surface EMG signals detected from the anal sphincter. Similar signals have been shown in detail in [18][19].
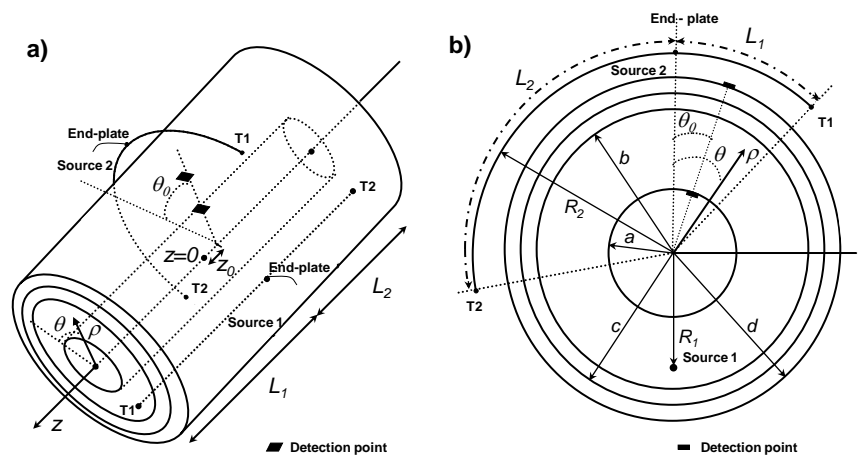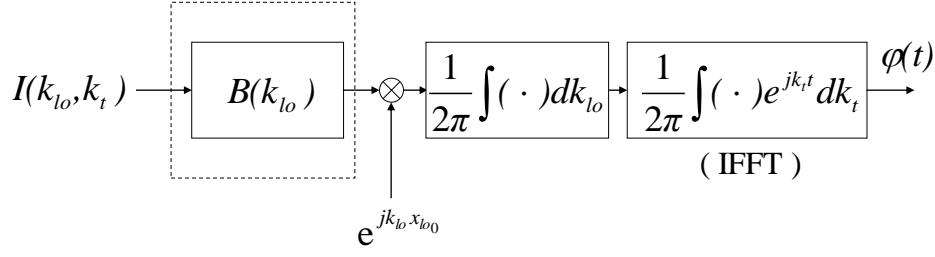
Figure 1

a)

End-plate
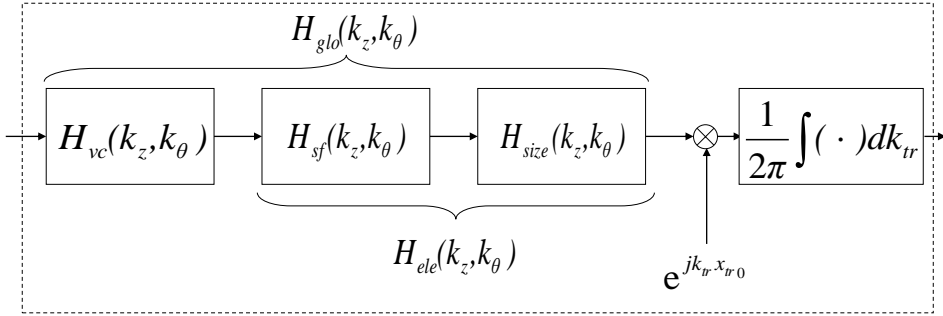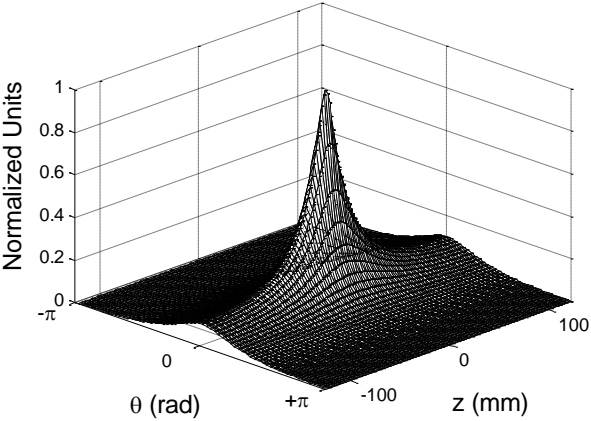Source 2
θ_0
T1
T2
z=0
z_0
End-plate
T2
Source 1
L_2
θ ρ
z
T1
L_1
▰ Detection point

b)

End - plate
L_1
L_2
Source 2
θ_0
θ ρ
T1
b
R_2
a
T2
c
R_1
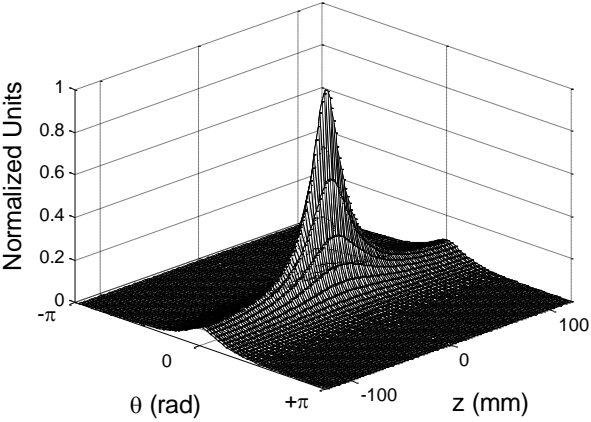d
Source 1
▬ Detection point

Figure 2

a)

b)

Figure 3

a)

b)

Figure 4

Figure 5

Figure 6